Biosensors and Bioelectronics 299 (2026) 118433

Contents lists available at ScienceDirect

Biosensors and Bioelectronics

journal homepage: www.elsevier.com/locate/bios

Roll-to-roll printed in-pad biosensors for colorimetric detection of key biomarkers in artificial vaginal fluid

Ziheng Wang [a], Semin Kwon [b], Tianhao Yu [a], Yumin Dai [c], Young L. Kim [b], Chi Hwan Lee [a,b,c,d,e,*]

[a] School of Mechanical Engineering, Purdue University, West Lafayette, IN, 47907, USA
[b] Weldon School of Biomedical Engineering, Purdue University, West Lafayette, IN, 47907, USA
[c] School of Materials Engineering, Purdue University, West Lafayette, IN, 47907, USA
[d] Elmore Family School of Electrical and Computer Engineering, Purdue University, West Lafayette, IN, 47907, USA
[e] Manufacturing and Materials Research Laboratories, Purdue University, West Lafayette, IN, 47907, USA

ARTICLE INFO

Keywords:
Roll-to-roll printing
Fabric fluidic device
Women health monitoring
Colorimetric sensing

ABSTRACT

Gynecological conditions often lack accessible, non-invasive diagnostic tools, leading to delayed detection and treatment, especially in resource-limited settings. Vaginal discharge and menstrual blood offer abundant but underutilized biomarkers for diagnosing gynecological disorders. Although sanitary pads represent an ideal platform for continuous fluid monitoring, direct high-throughput fabrication of sensors onto commercial pads remains challenging. Here, we introduce a roll-to-roll (R2R) wax-printing method optimized for large-scale production of fluidic colorimetric sensor patches designed for integration into sanitary pads. Utilizing specially formulated wax inks, this scalable approach enables consistent, cost-effective sensor fabrication. The sensor patches were functionalized with colorimetric reagents, incorporating enzymatic sensing elements for uric acid and glucose and physicochemical indicators for pH and moisture. This configuration enabled robust multi-analyte detection with clear and interpretable visual outputs, observable directly by the naked eye or via smartphone-based analysis. Validation in artificial vaginal fluid (AVF) confirmed reliable sensor performance, underscoring a practical and scalable platform with potential to advance proactive women's health monitoring in both home-based and point-of-care settings.

1. Introduction

Gynecological diseases represent a significant global health burden, affecting women across various stages of life (Cao et al., 2024; Gil-Ibanez et al., 2023). Many of these conditions remain undiagnosed, unacknowledged, or unreported for years, leading to delayed detection and treatment, particularly in resource-limited regions (Black and Fraser, 2012; Di Fiore et al., 2021). These diseases commonly manifest with debilitating symptoms such as heavy menstrual bleeding, chronic pelvic pain, and recurrent vaginitis, all of which can substantially impair daily functioning and overall quality of life (Wijeratne et al., 2024). Without timely intervention, these conditions may progress to more severe outcomes, including endometriosis, infertility, and gynecological cancers (GCs) (Baker-Rand and Kitson, 2024; Luo et al., 2025). Globally, gynecologic cancers account for a substantial and growing disease burden, with incidence rates projected to continue rising, which underscores the urgent need for accessible and effective diagnostic strategies. (Liang et al., 2025; Zhu et al., 2024).

Current diagnostic approaches for gynecological conditions often rely on invasive procedures, specialized laboratory infrastructure, and high operational costs, limiting their feasibility for routine or continuous monitoring (Di Fiore et al., 2021; Eskandar, 2024). In contrast, vaginal discharge and menstrual blood offer non-invasive, accessible sources of biomarkers relevant to both reproductive and metabolic health (Whitbread et al., 2024; Zaheer et al., 2024). Vaginal discharge is especially informative, reflecting changes in the local microbiome, pH balance, hormonal regulation, and infection status, while menstrual blood provides complementary insights into both localized and systemic physiological states (Kalantar-Zadeh et al., 2024; Saraf et al., 2021). Despite their diagnostic potential and routine availability, these

This article is part of a special issue entitled: Transformative bio-medical sensors published in Biosensors and Bioelectronics.

* Corresponding author. School of Mechanical Engineering, Purdue University, West Lafayette, IN, 47907, USA
E-mail address: lee2270@purdue.edu (C.H. Lee).

https://doi.org/10.1016/j.bios.2026.118433
Received 29 April 2025; Received in revised form 15 December 2025; Accepted 20 January 2026
Available online 26 January 2026

biological fluids remain underutilized in clinical practice and biomedical research (Dosnon et al., 2025). This underuse represents a missed opportunity to integrate low-barrier, sample-based health monitoring into everyday healthcare for women.

Recent efforts have advanced vaginal and menstrual biosensing technologies for point-of-care diagnostics, addressing a range of gynecological and reproductive health indicators (Dosnon et al., 2025; Kalantar-Zadeh et al., 2024). Reported platforms have targeted pH, microbial pathogens, and clinically relevant protein biomarkers such as C-reactive protein (CRP) and cancer antigen 125 (CA-125) (Dosnon et al., 2025; Paghi et al., 2023; Pal et al., 2020; Prabhu et al., 2021; Stojanović et al., 2025; Zhang et al., 2020). These approaches employ colorimetric, electrochemical, and optical strategies, demonstrated in formats including knitting threads, vaginal rings and lateral flow assays. Although these efforts have demonstrated important proof-of-concept capabilities, most remain restricted to laboratory-scale fabrication methods that are incompatible with large-scale hygiene product manufacturing or rely on external power sources that limit real-world applicability. By contrast, current commercial test strips are primarily single-analyte devices—predominantly pH-based—and require active user sampling, thereby lacking multiplexing and continuous monitoring capabilities (Shen et al., 2021). Recent studies demonstrate the growing potential of integrating flexible biosensors with smartphone-assisted colorimetric analysis, opening new possibilities for quantitative and user-friendly health monitoring (He et al., 2021; Li et al., 2024). Together, these advancements exemplify the convergence of flexible electronics, mobile imaging, and interface engineering, paving the way for practical, at-home colorimetric biosensing platforms amenable to large-scale translation.

Here, we introduce a high-throughput roll-to-roll (R2R) wax-printing technique tailored for large-scale manufacturing of fluidic colorimetric sensor patches for integration into sanitary pads. Unlike previous approaches restricted to small-scale, laboratory-based fabrication, our method enables reproducible, high-throughput production of wax-patterned fluidic structures. Using specially formulated wax inks, hydrophobic microfluidic patterns are directly formed on flexible polyester/cellulose fabric substrates. The continuous, single-step printing process achieves a throughput exceeding 10 impressions per minute with a channel resolution of ~300 μm, without requiring post-curing. This scalability ensures consistent quality, reduces unit cost, and provides a practical pathway toward clinical translation in hygiene product manufacturing. After fabrication, the fluidic patches are functionalized with colorimetric reagents for simultaneous detection of biomarkers including pH, moisture, uric acid, and glucose. The sensing reagents were stabilized within PVA/chitosan matrices to preserve activity and prevent leaching. To further ensure biosafety, the functionalized patch was encapsulated between medical-grade films with defined inlet and outlet openings. This multilayer configuration prevents direct contact between sensing chemistries and the skin, while directing fluid exclusively through the designated inlet to the sensing zone to ensure controlled flow and minimize potential exposure. Comparable multilayer encapsulation strategies have also been reported in previous wearable biosensing studies, reinforcing both the safety and practicality of our design (Zheng et al. 2023, 2024).

To validate the analytical performance of the fluidic sensor patch, artificial vaginal fluids (AVF) were prepared and tested under controlled conditions. The experimental results demonstrated a strong correlation with standard measurements, confirming the accuracy and reliability of the sensor response. The patches enabled rapid (within 10 min), visually interpretable results, which could be assessed either by the naked eye or quantified using a regression model applied to smartphone images. This dual-readout capability enhances accessibility and supports real-time health monitoring. Our approach presents a meaningful step toward improving women's health diagnostics by integrating multiplex biomarker detection with a scalable, cost-effective fabrication process. This platform offers the potential to help address diagnostic disparities and support early detection and management of gynecological and metabolic conditions in both home-based and point-of-care settings.

2. Experimental section

2.1. Chemicals

Chitosan powder, methanol, ethanol, uric acid, glucose, acetic acid, phenol red, polyvinyl alcohol (PVA), cobalt chloride, glucose oxidase (GOD), horseradish peroxidase (HRP), boric acid, phosphoric acid, 2-(N-morpholino)ethanesulfonic acid (MES), sodium phosphate, and sodium phosphate dibasic were purchased from Sigma-Aldrich. 3,3′,5,5′-Tetramethylbenzidine (TMB), 3,5-dichloro-2-hydroxybenzenesulfonic acid sodium salt (DHBS), 4-aminoantipyrine (4-AAP), 10,12-docosadiynedioic acid (DCDA), ethyl cellulose (EC), beeswax, Texanol (TEX), 2-butoxyethyl acetate (BEA), cyclohexanone (CYC), methyl isobutyl ketone (MIBK), and tetrahydrofuran (THF) were purchased from Fisher Scientific. Uricase was obtained from RayBiotech. LF1, MF1, Fusion 5 blood filters, and Grade 3 filter papers were purchased from Whatman. D23 grade blood filters were obtained from I.W. Tremont. Various fabric substrates, including 50/50 polyester/cotton (140 ± 15 μm thick), 80/20 polyester/cotton (200 ± 25 μm thick), 65/35 polyester/cotton (230 ± 12 μm thick), 45/55 polyester/cellulose (275 ± 16 μm thick), and 100 % polyester (340 ± 23 μm thick), as well as dark blue wax dye and brilliant pink ink, were obtained from Amazon.

2.2. Preparation of wax inks

Wax ink was formulated based on established protocols and further optimized for improved performance (Tzianni et al., 2024). Briefly, 50 % w/v wax solutions were prepared by dissolving wax in individual solvents, including Texanol (TEX), benzyl ethyl acetate (BEA), and cyclohexanone (CYC) at 97 °C, methyl isobutyl ketone (MIBK) at 85 °C, and tetrahydrofuran (THF) at 65 °C, using separate oil baths. Upon complete dissolution, each solution was cooled to room temperature under continuous stirring and left overnight prior to further processing. Ethyl cellulose (EC) solutions were prepared by gradually adding EC to each solvent under vigorous stirring until a clear solution was obtained. Final EC concentrations were determined by solubility limits: 4 % w/v for TEX, 6 % w/v for CYC, and 8 % w/v for BEA, THF, and MIBK.

Wax inks were prepared by mixing 30 g of wax solution with 20 g of the corresponding EC solution and 0.05 g of wax dye, followed by homogenization using a Thinky mixer. This mixing process was repeated as necessary to achieve the desired rheological properties. For mixed-solvent wax inks, BEA and TEX were premixed at volume ratios of 9:1, 8:2, and 7:3, stirred for 2 h before preparing the respective wax and EC stock solutions. In these cases, EC was used at a final concentration of 8 % w/v. Wax inks were subsequently prepared using the same procedure. All wax inks were stored in sealed containers at 20 °C and re-homogenized using a Thinky mixer prior to each printing session.

2.3. Characterizations of wax ink

Rheological behavior of the wax inks was characterized using a TA Instruments DHR-3 rheometer. SEM imaging was conducted with a Hitachi S-4800 field emission scanning electron microscope (FE-SEM) on sputter-coated samples. Optical cross-sectional images of the wax barriers were captured using a Nikon Eclipse LV150N microscope. Clogging time was evaluated during continuous printing at a speed of 6 m/min, defined as the time from wax ink loading until the appearance of noticeable pattern defects.

To assess barrier formation, samples with 1–6 sequential print cycles using different ink formulations were fabricated, left overnight to allow complete solvent evaporation, and subsequently tested by applying 6 μL of an aqueous dye solution. The minimum number of printing cycles required to achieve a leak-proof wax barrier was determined based on

the dye confinement performance.

2.4. R2R printing and evaluation of the fluidic pattern

Screen masks were obtained from NBC Meshtec, and a nonwoven fabric dressing was used as the printing substrate. A photograph of the screen mask design used for R2R printing is provided in Fig. S1. Dummy prints were initially conducted to ensure proper alignment and print quality prior to automated production. Continuous R2R printing was carried out at a speed of 6 m/min. Fluidic patterns of three different sizes (design details shown in Fig. S2) were screen-printed and pre-dried inline using an alternating airflow system for 10 min. The printed roll was then rewound and subjected to further drying at a reduced speed of 2 m/min. Following printing and drying, the fabric was conditioned under ambient conditions for 24 h before use.

Printing resolution was evaluated using fluidic patterns with channel widths ranging from 150 to 500 μm and barrier widths from 200 to 600 μm. Ink leakage resistance was assessed by dispensing 3 μL of an aqueous dye solution into the sample zone and monitoring lateral diffusion. For sensor color calibration purposes, a microzone pattern was designed and fabricated, consisting of barriers with a width of 1.5 mm and a radius of 2 mm.

2.5. Preparation and loading of colorimetric biosensing reagents

Five colorimetric sensors were prepared for the detection of pH, uric acid, glucose, and moisture. The reversible pH sensor was fabricated by dissolving 0.04 wt% phenol red in a 2 wt% PVA solution. The irreversible pH sensor was prepared by dissolving 2 mM 10,12-docosadiynedioic acid (DCDA) in ethanol, followed by sonication for 1 h. The solution was then polymerized under 254 nm UV irradiation for 60 s and subsequently blended at a 3:1 ratio with 1 mg/mL chitosan solution in 0.25 % (v/v) acetic acid. The moisture sensor was fabricated by dissolving cobalt chloride ($CoCl_2$) at 100 mg/mL in a 2 wt% PVA solution.

The uric acid and glucose sensors were fabricated using a multilayer deposition strategy. First, 1 mg/mL chitosan solution prepared in 0.25 % (v/v) acetic acid was deposited onto the substrate. For the uric acid sensor, a chromogenic reagent solution containing 4 mM 4-aminoantipyrine (4-AAP) and 8 mM 3,5-dichloro-2-hydroxybenzenesulfonic acid (DHBS) was added, followed by deposition of 0.15 mg/mL horseradish peroxidase (HRP) solution prepared in Britton-Robinson (B-R) buffer at pH 5.6, and 80 U/mL uricase prepared in B-R buffer at pH 8.5. For the glucose sensor, 15 mM 3,3′,5,5′-tetramethylbenzidine (TMB) dissolved in methanol was used as the chromogenic reagent, followed by 0.15 mg/mL HRP in B-R buffer at pH 5.6, and 170 U/mL glucose oxidase (GOD) prepared in B-R buffer at pH 7.0. In both sensors, the chromogenic reagent was re-applied after the enzyme layers. Each deposited layer was allowed to dry completely at room temperature under controlled light conditions before the addition of the next layer. Detailed chemical loading volumes corresponding to different fluidic pattern sizes are provided in Fig. S2.

2.6. Assembly of the sensor patch

The 3M Tegaderm film and medical silicone tape were pre-cut using a hole punch to create circular openings for the inlet and outlet regions. Various blood filter papers were similarly punched to form circular layers. The reagent-loaded fabric was cut to size, stacked with the blood filter positioned above the inlet, and then sandwiched between the top 3M Tegaderm transparent film and the bottom 3M medical silicone adhesive tape.

2.7. Preparation of buffers and AVFs

A universal buffer system was used to prepare a pH calibration series ranging from pH 5.0 to 12.0. The buffer consisted of 0.04 M each of boric acid (H_3BO_3), phosphoric acid (H_3PO_4), and acetic acid (CH_3COOH) dissolved in distilled water. Individual buffer solutions were adjusted to target pH values (4.0, 5.0, 6.0, 7.0, 8.0, 9.0, 10.0, and 11.0) by titrating with 0.2 M sodium hydroxide (NaOH) under continuous stirring, with pH monitored using a calibrated pH meter. All buffers were prepared in 0.9 % NaCl to maintain ionic strength, filter sterilized through a 0.22 μm membrane, and stored at 4 °C. Solutions were equilibrated to room temperature prior to use in calibration measurements.

For uric acid sensor calibration, a series of uric acid solutions (0, 0.02, 0.04, 0.08, 0.1, 0.2, 0.4, 0.6, 0.8, 1.0, and 2.0 mM) was prepared in 10 mM phosphate buffer (pH 6.8) containing 0.9 % NaCl. Uric acid was precisely weighed and dissolved in pre-warmed (37 °C) buffer under gentle stirring to aid solubilization. Each concentration was prepared in 100 mL total volume, filter sterilized (0.22 μm), and stored at 4 °C for use within 48 h to maintain stability.

Similarly, a glucose calibration series (0, 0.02, 0.04, 0.08, 0.1, 0.2, 0.4, 0.6, 0.8, 1.0, 2.0, 3.0, and 4.0 mM) was prepared by dissolving D-glucose directly in 10 mM phosphate buffer (pH 6.8) with 0.9 % NaCl at room temperature. Solutions were stirred until fully dissolved, filter sterilized (0.22 μm), stored at 4 °C, and used within one week to avoid degradation and microbial contamination.

Artificial vaginal fluid (AVF) was prepared following a modified protocol from established formulations (Owen and Katz, 1999). Briefly, 1 L of the simulant contained (in g): NaCl, 3.51; KOH, 1.40; $Ca(OH)_2$, 0.222; bovine serum albumin, 0.018; lactic acid, 2.00; acetic acid, 1.00; glycerol, 0.16; and urea, 0.40. Two variants were designed to represent healthy (AVF-H) and pathological (AVF-P) vaginal secretions. AVF-H was adjusted to pH 5.0, and AVF-P to pH 7.4 using NaOH and HCl solutions. Glucose and uric acid were added to achieve final concentrations of 0.2 mM and 0.1 mM for AVF-H, and 4.0 mM and 4.0 mM for AVF-P, respectively. All components were dissolved in distilled water, stirred at 37 °C until completely dissolved, and stored at 4 °C until use.

2.8. Color analysis and sensor calibration

For linear model calibration, images of the sensor patches were captured before analyte addition to serve as the background, using a smartphone under white light conditions. After analyte addition, the sensor patches were allowed to react and stabilize for 10 min, after which images were captured again. The images were analyzed using ImageJ software to extract RGB values, saturation, and grayscale intensities. Using the “HSB Stack Splitter” plugin, each image was separated into hue, saturation, and brightness components. The intensity of the saturation images was further analyzed using the Color Histogram plugin. Differences between pre- and post-analyte addition images were used to calculate ΔSaturation and ΔGray Value for each sensor patch. The limits of detection (LODs) for each sensor were calculated from the regression equation at a signal of $S \pm 3\sigma$, where S is the signal of blank and σ is standard deviation of the blank.

For AVF sample quantification, images of the colorimetric sensors were captured alongside a Macbeth ColorChecker using a smartphone (Samsung Galaxy S21, PRO mode) under variable color temperatures of 3000 K and 5800 K with auto white balance enabled. Regression-based color correction, a widely adopted approach in colorimetric analysis, was applied to enhance the accuracy of the sensor readouts (Akkaynak et al., 2014; Bianco et al., 2013; Finlayson et al., 2015; Hung, 1993; Pascale, 2006). Detailed procedures for color correction are provided in the Supplementary Information.

3. Results and discussion

3.1. Design and fabrication of sensor patch

Fig. 1A illustrates the colorimetric sensor patch designed for seamless integration into a sanitary pad for women's health monitoring. The sensor produces distinct colorimetric responses discernible to the naked

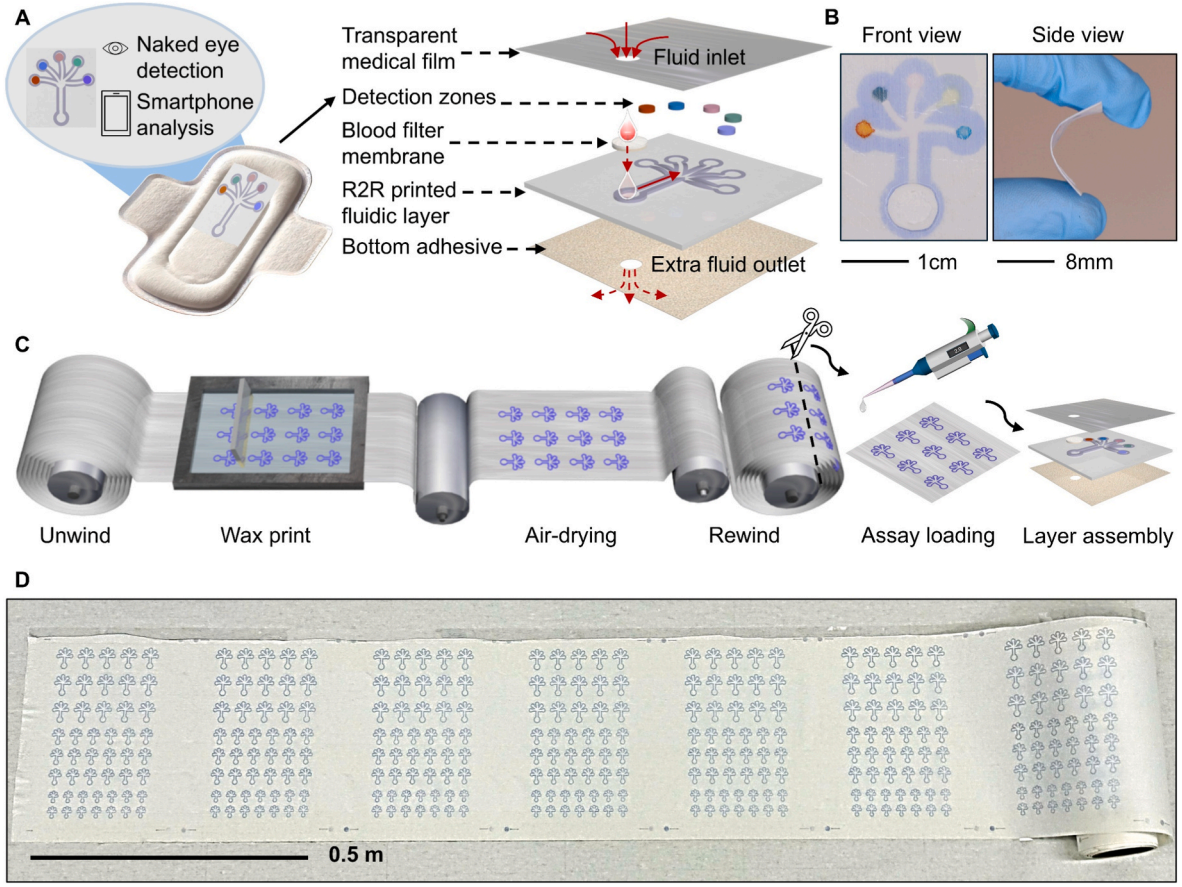

Fig. 1. Roll-to-roll (R2R) fabrication and device configuration of the fabric-based colorimetric sensor patch. (A) Schematic illustration of the final device configuration integrated into a sanitary pad, highlighting the fluid inlet, sensing zones for multiplexed biomarker detection, fluid outlet, and capability for naked-eye and smartphone-based analysis. (B) Front view and side view of the sensor patch. (C) Schematic of the R2R screen printing and multilayer assembly process for sensor patch fabrication. (D) Photograph of large-area fabric rolls showing uniform printing of fluidic sensor arrays.

eye, which can be quantitatively analyzed using a smartphone camera in combination with a standardized color checker to ensure calibration accuracy. The R2R wax-printed fabric microfluidic layer guides vaginal fluid from the inlet toward the sensing zone. A plasma-separating blood filter membrane (D23) is precisely cut and positioned over the inlet to enable efficient separation of particulates. The fluidic assembly is encapsulated between a transparent 3M Tegaderm medical film and a medical-grade adhesive backing, both pre-punched with aligned circular inlets to facilitate controlled fluid entry while shielding the sensing reagents from external contamination.

The middle fabric microfluidic layer, patterned with wax ink, comprises a central sensing region connected via a longitudinal channel to five discrete detection zones, enabling multiplexed biomarker analysis and flexible sensor configuration. The transparent top film allows real-time visualization and accurate imaging of colorimetric transitions, whereas the bottom adhesive layer ensures stable attachment to the pad substrate. This dual encapsulation design effectively isolates the sensing reagents from direct bodily contact and mitigates environmental interference. Among the five membranes evaluated (Fig. S3), the D23 blood filter exhibited the highest efficiency in red blood cell removal, preventing blood-induced color interference in the sensing region. Front and side views of the assembled patch further demonstrate its lightweight, thin, and conformable structure suitable for integration into commercial sanitary products (Fig. 1B).

Fig. 1C illustrates the complete fabrication process of the sensor patch. The middle fabric microfluidic layer was produced using a Kinzel R2R platform equipped with a vacuum-assisted conveyor system, enabling fully automated, continuous, and high-precision in-line operation. This process supports high-throughput manufacturing, achieving over six impressions per minute, with each impression containing 47 individual fluidic patterns. Using a wax-based screen-printable ink, continuous fabrication exceeding 76 m was completed within approximately 50 min. The R2R workflow comprises sequential unwinding of the fabric roll, screen printing of fluidic patterns, dual-stage in-line drying with alternating airflow, and rewinding of the finished material (Movie S1). A representative 1.5 m segment of the R2R-fabricated fabric is shown in Fig. 1D, with an extended overview provided in Fig. S4 to highlight the scalability of the process. The high-throughput and material-efficient nature of this approach enables cost-effective production of disposable sensing patches for at-home women's health monitoring. Based on current retail prices of the ink components, the estimated material cost was approximately $0.33 per imprint and $0.007 per individual fluidic unit (Table S1). Three fluidic pattern geometries of varying sizes were developed to accommodate different volumes of vaginal secretions and user needs, with dimensional details summarized in Fig. S2.

Supplementary video related to this article can be found at https://doi.org/10.1016/j.bios.2026.118433

3.2. Colorimetric sensor development and calibration

Fig. 2A illustrates the five colorimetric sensing elements integrated into the wax-printed fabric microfluidic layer in a clockwise arrangement: a reversible pH sensor (R. pH), an irreversible pH sensor (IR. pH), a uric acid sensor, a glucose sensor, and a moisture sensor. These biomarkers were strategically selected to capture key indicators of vaginal

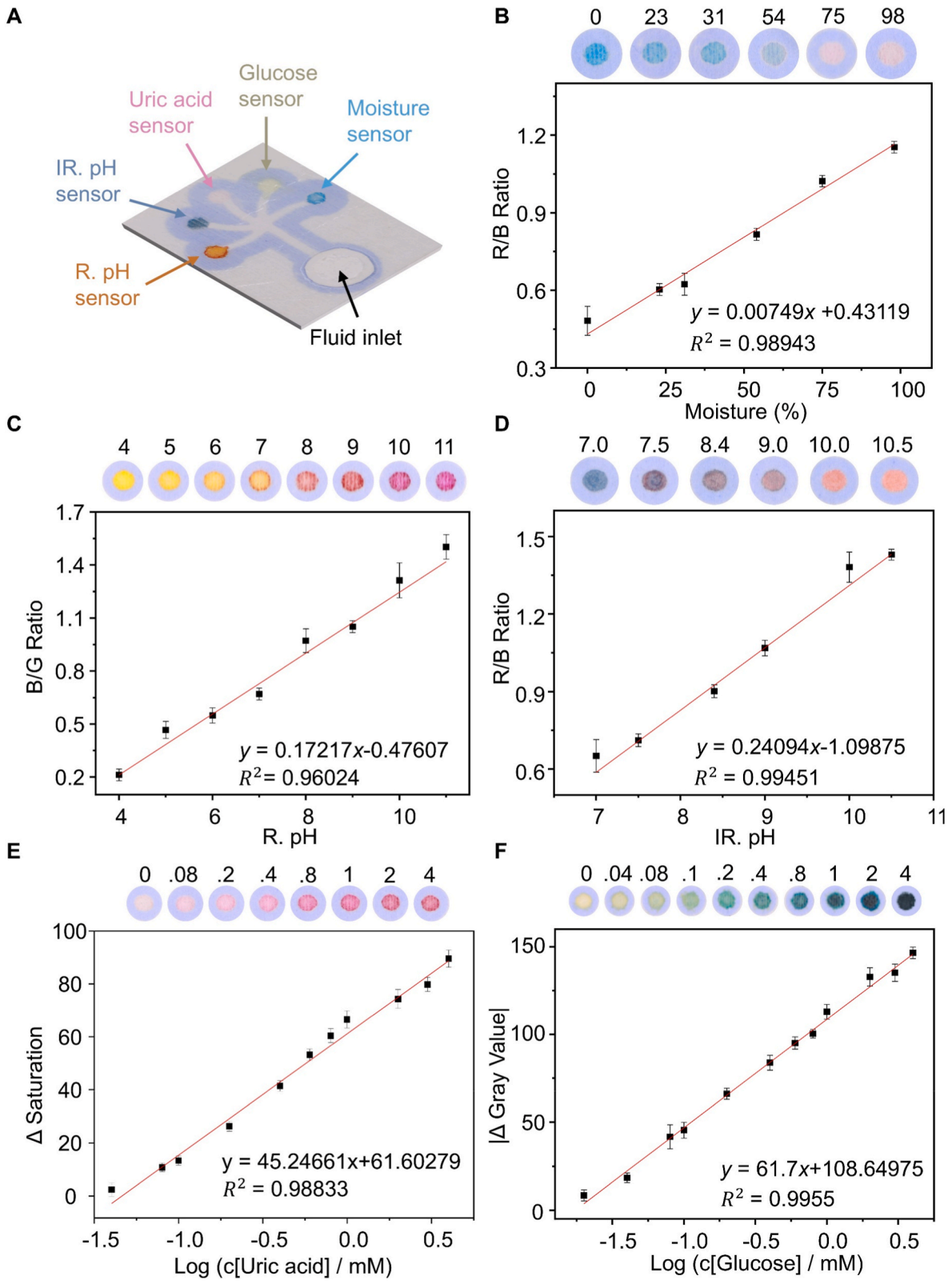

Fig. 2. Characterization and calibration of the colorimetric sensors. (A) Layout of the five colorimetric sensors integrated into the wax-printed fluidic patch, designed for reversible pH, irreversible pH, uric acid, glucose, and moisture detection. (B) Calibration of the moisture sensor across relative humidity levels from 0 to 100 %. (C) Calibration of the reversible pH sensor over the pH range of 4.0–11.0. (D) Calibration of the irreversible pH sensor in response to increasing pH. (E) Calibration of the uric acid sensor across concentrations of 0–4.0 mM. (F) Calibration of the glucose sensor across concentrations of 0–4.0 mM. Error bars in (B–F) represent the standard deviation (SD) from three independent sensors.

health. Vaginal pH serves as a primary diagnostic parameter, normally maintained between 3.8 and 5.0 to preserve an acidic environment that suppresses pathogenic growth; elevated pH levels are commonly associated with bacterial vaginosis and related infections (Lin et al., 2021b). Beyond pH, vaginal metabolites reflect both local and systemic physiological changes (Kalantar-Zadeh et al., 2024; Paghi et al., 2023). Although glucose concentrations in vaginal secretions are typically low, elevated levels have been linked to diabetes and vulvovaginal candidiasis (Maduta et al., 2024; Navarro et al., 2023). Similarly, increased uric acid may result from urinary leakage due to elevated bladder pressure, a symptom associated with interstitial cystitis (Lin et al., 2021a). Vaginal moisture is highly condition dependent, reflecting the balance between epithelial transudation, glandular secretion, and inflammatory exudate. Reduced lubrication is commonly associated with hypoestrogenic or atrophic states, whereas infectious and inflammatory conditions such as bacterial vaginosis and candidiasis are characterized by increased vaginal discharge and elevated moisture relative to healthy baseline conditions (Gabrieli et al., 2022; Kairys et al., 2024; Stabile et al., 2021). In this work, the moisture sensor serves as a contextual indicator of hydration state, designed to distinguish low versus high hydration regimes relevant to these conditions. In addition, moisture sensing plays a functional role by indicating sufficient fluid availability for complete sensor wetting and reliable colorimetric signal development. The clinical relevance of each biomarker is summarized in Table S2.

Different sensing chemistries were employed to achieve distinct and quantifiable colorimetric responses for each biomarker. Fig. 2B–F show the calibration curves correlating normalized colorimetric ratios with analyte concentrations. The moisture sensor was prepared by embedding cobalt chloride in a PVA matrix, where increasing moisture levels induced a visible color transition from blue to pink. The corresponding red-to-blue (R/B) ratio exhibited a strong correlation across the 0–100 % relative humidity range, yielding a limit of detection (LOD) of 23 % (Fig. 2B). The reversible pH sensor was fabricated by incorporating phenol red into a PVA matrix. Phenol red was selected for its pronounced chromatic shift near physiological pH, transitioning from yellow to red to magenta as pH increased. The PVA network provided mechanical stabilization, minimized dye leaching, and enhanced color uniformity during fabrication. The R/B ratio demonstrated a strong linear response from pH 4–11 with a resolution of approximately 0.5 pH units, and an LOD of pH 4.0 (Fig. 2C). The irreversible pH sensor was constructed by embedding polydiacetylene (PDA) vesicles in a chitosan matrix. The PDA backbone undergoes an irreversible electronic transition under alkaline conditions: at low pH, the intact π-conjugated structure maintains a stable blue color, whereas increasing pH disrupts conjugation through electrostatic repulsion, yielding an irreversible blue-to-orange shift. The R/B ratio correlated well across the pH 7–10.5 range with a resolution of approximately 0.2 pH (Fig. 2D). This irreversible response provides a visual indication of sustained alkaline exposure, serving as an alert for potential pathological conditions during patch wear.

The uric acid and glucose sensors were fabricated through an enzyme cascade reaction using a multilayer modification approach. Each sensing zone was first coated with a chitosan matrix to enhance enzyme immobilization, maintain catalytic activity, and improve colorimetric clarity. Chromogenic reagents (4-AAP with DHBS for uric acid and TMB for glucose) were then incorporated, with each substrate yielding a distinct color change specific to its analyte. HRP and the respective oxidases (uricase for uric acid and glucose oxidase (GOD) for glucose) were then immobilized to catalyze the target-specific reactions. A second deposition of chromogenic reagents was applied to enhance signal intensity. Upon exposure to target analytes, enzymatic oxidation by uricase or GOD generates hydrogen peroxide (H_2O_2), which is then reduced by HRP, initiating chromogenic oxidation and producing visible color transitions proportional to analyte concentration. As shown in Fig. 2E and F, the uric acid sensor exhibited a color change from colorless to pink, while the glucose sensor transitioned from colorless to blue. The changes in saturation and absolute gray value displayed linear relationships with the logarithm of analyte concentration. The uric acid sensor demonstrated a linear range of 0–4 mM with a limit of detection (LOD) of 0.04 mM, whereas the glucose sensor showed a linear range of 0–4 mM with an LOD of 0.03 mM.

To ensure accurate and consistent colorimetric quantification, sensor patches were photographed under ambient illumination alongside a standardized Macbeth ColorChecker (Fig. S5A). The captured RGB values were processed using a regression-based color correction model that converts device-dependent RGB inputs into device- and lighting-independent CIE XYZ values. A polynomial transformation framework was trained using the ColorChecker reference to establish a robust mapping between the captured RGB data and their corresponding CIE XYZ coordinates. This method, previously developed and validated by our group (Park et al., 2025; Wang et al., 2025), demonstrated strong robustness against variations in illumination, camera type, and user handling. The same approach was applied here to enable reliable biomarker quantification from the colorimetric fluidic patch under typical at-home lighting conditions. The corrected chromatic data, visualized in the CIE 1931 color space (Fig. S5B–F), verified the high color fidelity and quantitative accuracy of the pH, moisture, uric acid, and glucose sensors.

The storage stability of the sensors was evaluated under typical storage conditions (Fig. S6). The non-enzymatic sensors, including the reversible pH, irreversible pH, and moisture sensors, exhibited stable colorimetric responses with negligible drift over at least 1 month at room temperature. In contrast, the enzyme-based uric acid and glucose sensors showed gradual activity decay, retaining approximately 86 % and 89 % of their initial responses, respectively, after one week of storage in sealed Petri dishes at ambient temperature. These results indicate that non-enzymatic platforms offer excellent intrinsic stability, whereas the operational lifetime of enzymatic sensors is primarily limited by enzyme deactivation. Consistent with previous reports, refrigerated storage (4 °C) has been shown to mitigate enzymatic degradation and can serve as a practical means to extend the shelf-life of enzyme-based colorimetric systems (Nguyen et al., 2019; Puggioni et al., 2019).

3.3. Development and optimization of the wax ink

To construct stable and high-resolution fluidic barriers on fabric substrates, wax inks were formulated and optimized for continuous R2R screen printing. Five solvents (Texanol, 2-butoxyethyl acetate, cyclohexanone, methyl isobutyl ketone, and tetrahydrofuran) were initially selected based on two key criteria: (1) strong solubility for wax materials to ensure homogeneous ink preparation, and (2) established use in screen printing inks due to their suitable evaporation rates, viscosity control, and process compatibility. These properties are critical for achieving stable barrier formation on porous fabrics and maintaining reliable R2R operation (Ahmed et al., 2023; Kim et al., 2021; Tzianni et al., 2024).

Wax inks were prepared by dissolving wax in individual solvents and subsequently mixing with a polymer solution of ethyl cellulose (EC) to adjust viscosity. Final concentrations were determined by the solubility limit of EC in each solvent (details in Section 2.2). Fig. 3A shows the rheological behavior of the prepared wax inks, all exhibiting shear-thinning profiles typical of screen printing. The inset focuses on the shear rate range relevant to printing, where TEX- and BEA-based inks maintained relatively higher viscosities, supporting more stable ink transfer. In contrast, CYC-, MIBK-, and THF-based inks showed a pronounced viscosity decrease with shear rate, which could compromise print fidelity during continuous operation.

Continuous printing tests on polyester/cellulose fabrics revealed clear differences in clogging resistance (Fig. 3B). TEX-based inks exhibited the longest clogging time (72 min), followed by BEA (38 min), while CYC, MIBK, and THF showed much shorter times (26, 18, and

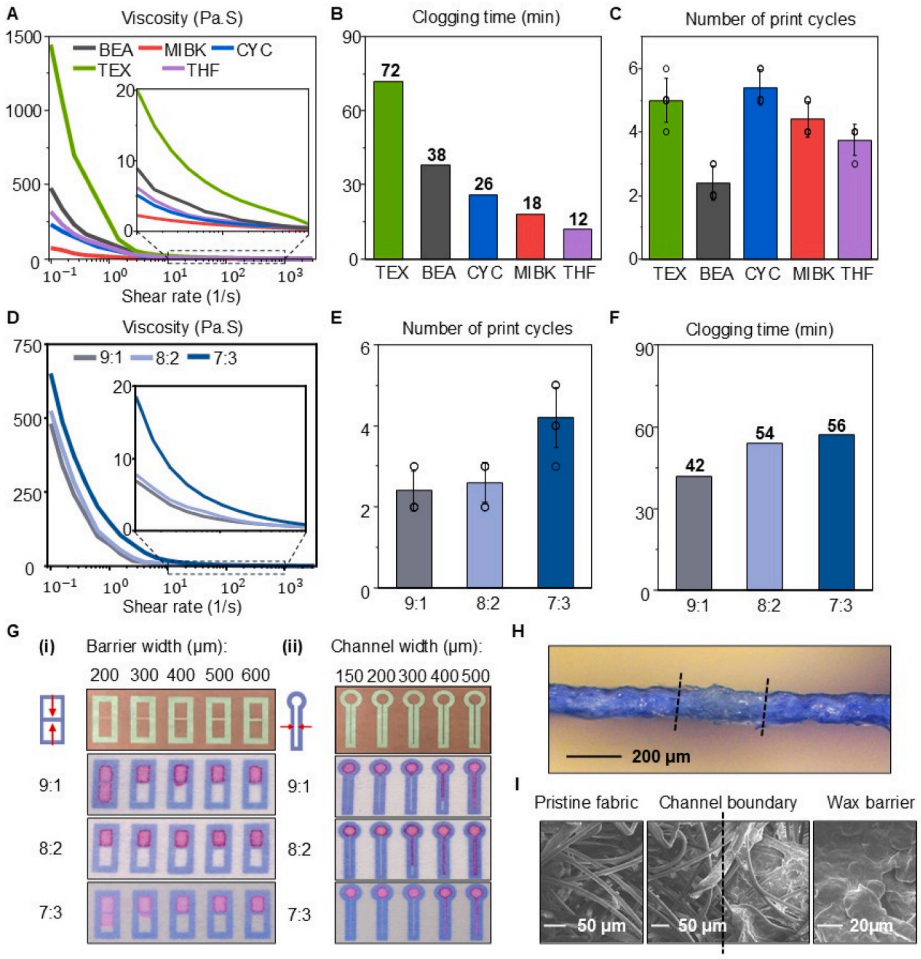

Fig. 3. Characterization of wax ink formulation, printing performance, and barrier resolution. (A) Rheological profiles of wax inks formulated with different solvents, showing shear-thinning behavior across operational shear rates. (B) Clogging time measurements for different solvent-based wax inks during continuous printing. (C) Number of print cycles required to form effective fluidic barriers. (D) Rheological behavior of mixed-solvent (BEA:TEX) wax inks with varying ratios. (E) Clogging time comparison for BEA:TEX inks at different ratios. (F) Number of print cycles required for effective barrier formation using BEA:TEX inks. (G) Printing resolution evaluation for barriers and channels with varying feature widths. (H) Cross-sectional optical image of a printed wax barrier embedded in the fabric substrate. (I) SEM images showing fabric morphology with and without wax barrier. Error bars in (C) and (E) represent the standard deviation (SD) from three independent batches of sensors.

12 min, respectively). These results correlate with the rheological profiles, indicating that higher viscosity stability at operational shear rates prolongs working time and reduces clogging. Barrier formation efficiency was further evaluated by counting the number of printing cycles required to create leak-proof channels using dyed aqueous solutions (Fig. 3C). TEX- and CYC-based inks required ~5 cycles, while MIBK and THF formed barriers in ~4 cycles. Notably, BEA-based inks achieved complete barrier formation within ~2 cycles, demonstrating superior spreading and material efficiency. A summary of solvent properties and ink performance is provided in Table S3.

Given the complementary advantages of TEX (high viscosity stability) and BEA (efficient barrier formation), mixed-solvent formulations were investigated. TEX was expected to improve printing stability, whereas BEA would promote faster barrier completion. Wax inks were prepared with TEX:BEA volume ratios of 9:1, 8:2, and 7:3. As shown in Fig. 3D, all mixed inks displayed shear-thinning behavior, with higher TEX content yielding higher viscosity. Printing performance was compared based on the number of cycles required for leak-proof barrier formation (Fig. 3E) and clogging time under continuous operation (Fig. 3F). The 8:2 TEX:BEA formulation offered the optimal balance, forming complete barriers in ~3 cycles while maintaining a clogging time of 54 min. The 9:1 mixture showed shorter working time (42 min), whereas the 7:3 mixture required more cycles (~5), demonstrating a trade-off between barrier efficiency and operational stability.

Printing resolution and wicking performance were further assessed using microfluidic patterns with varying channel and barrier widths (Fig. 3G). The 8:2 ink consistently produced sharply defined features, achieving minimum barrier widths of 200 μm and channel widths of 300 μm. Cross-sectional imaging (Fig. 3H) confirmed complete wax penetration and channel integrity, while SEM analysis (Fig. 3I) revealed uniform wax impregnation into the fabric structure. Based on these results, the 8:2 TEX:BEA ink was selected for all subsequent fluidic patterning.

Fig. 4A presents a schematic illustration of the R2R screen printing process used for wax barrier deposition, highlighting the critical roles of wax–polymer–solvent interactions in achieving stable and continuous fluidic barriers. To evaluate substrate effects, five fabrics of varying thickness were tested: 50/50 polyester/cotton (P/Cot), 80/20 P/Cot, 65/35 P/Cot, 45/55 polyester/cellulose (P/Cell), and 100 % polyester (P). Barrier quality was assessed through printing and dye-leakage testing (Fig. 4B). Thinner fabrics (<200 μm) such as 50/50 and 80/20 P/Cot enabled rapid penetration but suffered from excessive lateral spreading, leading to poor channel definition. With increasing fabric thickness, lateral diffusion decreased and feature definition improved, though more print cycles were required for full barrier formation (Fig. 4C and D). Among the tested substrates, the 45/55 P/Cell fabric

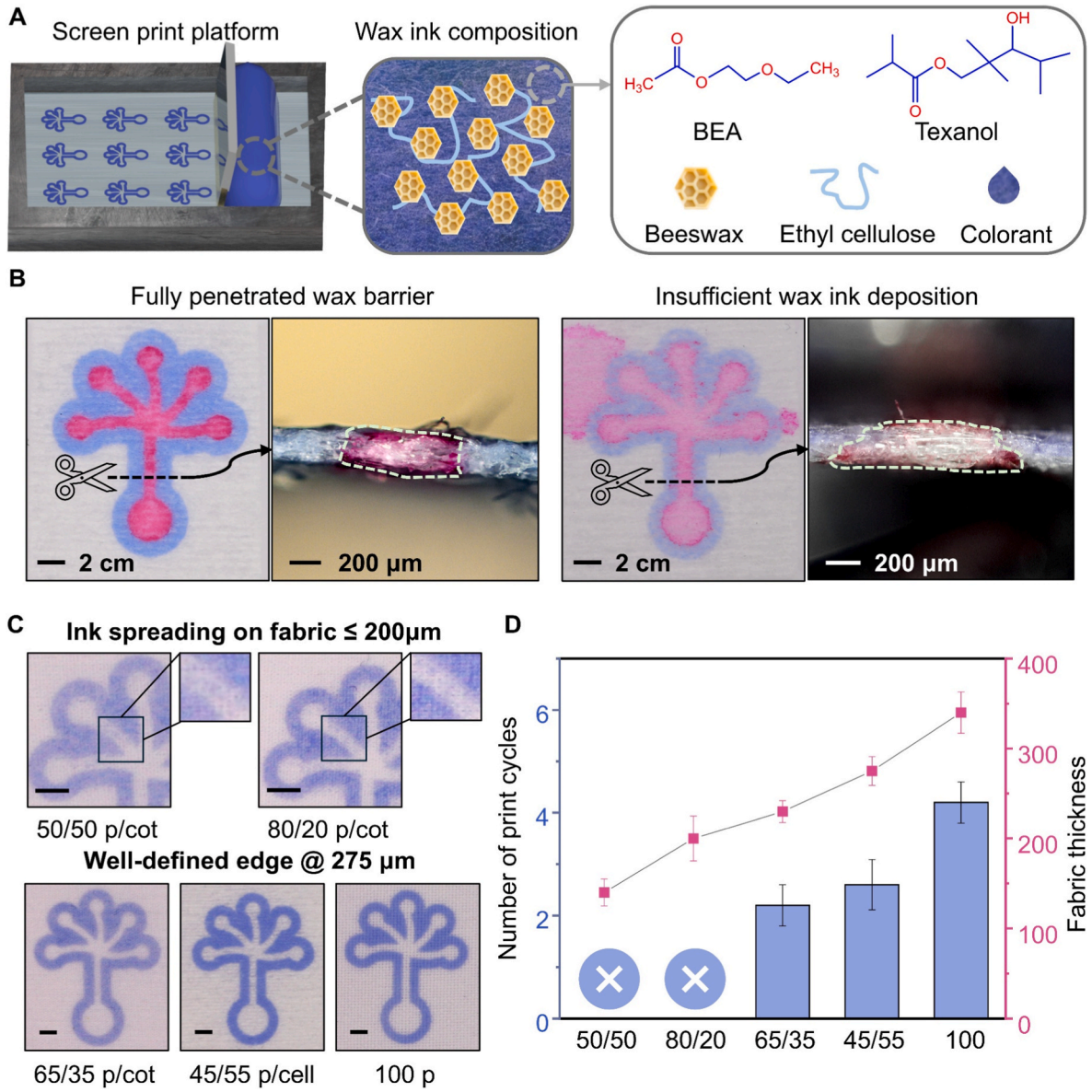

Fig. 4. Mechanism and performance characterization of wax barrier formation on fabric substrates. (A) Schematic illustration of the R2R printing process and molecular interactions between wax, polymer, and solvent within the fabric substrate. (B) Cross-sectional images showing fluid penetration profiles for effective and ineffective wax barrier formations. (C) Top-view and magnified images demonstrating barrier resolution on fabrics of varying thicknesses. Scale bars, 2 cm. (D) Analysis of the number of printing cycles required for effective barrier formation and its correlation with fabric thickness. Error bars represent the standard deviation (SD) from three independent batches of sensors.

(275 µm) provided the best balance, requiring only three print cycles to produce sharp, leakage-free microfluidic patterns. This substrate was therefore selected for device fabrication.

The fluidic performance of the R2R-fabricated devices is demonstrated in Fig. S7. All pattern sizes (small, medium, and large) exhibited rapid capillary-driven filling, reaching full saturation within 5 min for low-viscosity aqueous solutions. Fig. S7B highlights the patternability of the fabrication approach, demonstrating the ability to print complex shapes and maintain controlled fluid flow along the designed pathways without leakage. To assess wicking under physiologically relevant conditions, a viscous test fluid (0.5 wt% xanthan gum, ≈80 mPa s) was compared with the aqueous control (~1 mPa s). Despite slower advancement, the viscous fluid achieved complete filling within 30 min, confirming robust and consistent capillary-driven transport across viscosity ranges representative of menstrual and vaginal secretions.

To assess process reproducibility, pattern uniformity was evaluated across over 5 m of R2R-fabricated rolls (20 imprints, 47 units each). Six units per imprint were randomly selected for leakage and RGB uniformity testing (Fig. S8). Consistent barrier formation and channel integrity were observed throughout (Fig. S8A), with minimal RGB variation across imprints (Fig. S8B), indicating excellent fabrication consistency. Collectively, these results validate the optimized wax-ink formulation and R2R strategy as a scalable, high-resolution approach for fabric-based microfluidic device manufacturing.

3.4. Quantitative analysis of the sensor patch with AVFs

To evaluate the performance of the sensor patch for simultaneous detection of pH, uric acid, glucose, and moisture across clinically relevant ranges, two artificial vaginal fluid (AVF) formulations were prepared based on modified published protocols to represent healthy and pathological conditions (Owen and Katz, 1999). The AVF compositions were designed to approximate key physicochemical properties of vaginal secretions relevant to sensor performance, incorporating

physiologically relevant inorganic ions (Na^+, K^+, Ca^{2+}), bovine serum albumin as a protein component, organic acids (lactic and acetic acid), and glycerol to adjust viscosity and osmolarity. The healthy AVF (AVF-H) was adjusted to pH 5.0 and contained 0.2 mM glucose, 0.1 mM uric acid, and moderate moisture content, whereas the pathological AVF (AVF-P) was adjusted to pH 7.4 and contained 4.0 mM glucose, 4.0 mM uric acid, and elevated moisture. While the AVF formulations provide a controlled and reproducible environment for evaluating sensor response, they represent a simplified approximation of vaginal secretions. As a result, components such as additional metabolites, immune factors, and dynamic microbial activity, as well as inter-individual variability present in clinical samples, are not captured and should be considered when interpreting the current results.

To assess wettability and fluid interaction, water contact angle (WCA) measurements were performed on all five sensors fabricated on the 45/55 polyester/cellulose fabric substrate. This porous, hydrophilic fabric exhibited a control WCA of ~30°, facilitating rapid liquid absorption and distribution. The initial WCAs of the sensors ranged from 31.5° to 122° (Fig. S9). Although some sensors displayed higher initial angles, all showed rapid reduction in WCA due to continuous wicking. The reversible pH sensor (31.5°) demonstrated immediate wetting and a stable color response within 1 min, whereas the irreversible pH sensor (122°) required up to 10 min for full saturation. Measurements conducted in AVF showed similar trends, with all sensors ultimately yielding reproducible colorimetric signals within 10 min, confirming robust operation in both aqueous and biofluid environments.

All sensors exhibited strong specificity toward their respective biomarkers with negligible cross-reactivity to physiologically relevant interferents (Fig. S10). At pH 7, the B/G ratio of the reversible pH sensor (~0.63) and R/B ratio of the irreversible pH sensor (~0.6) remained unchanged in the presence of various analytes, confirming selective H^+ response. The moisture, uric acid, and glucose sensors also maintained stable outputs across varying ionic strengths and solute compositions, indicating that colorimetric signals were unaffected by coexisting species. The sensors further demonstrated excellent thermal stability: RGB responses for both AVF-H and AVF-P remained consistent at 25 °C and 40 °C (Fig. S11), underscoring the robustness of the sensing chemistries under environmental variations.

For quantitative analysis of sensor colorimetric responses, images of the sensor patch were captured 10 min after sample addition to ensure full color development (Fig. 5A). Distinct color transitions were observed across the five sensing zones under AVF-H and AVF-P conditions, clearly visible to the naked eye. The normalized quantitative data for pH, moisture, glucose, uric acid, and response time (Fig. 5B) were plotted on a 0–1 scale for direct comparison using a radar plot, revealing marked differences in biomarker profiles between healthy and pathological fluids.

Detailed colorimetric analysis (Fig. 5C) revealed characteristic responses for each sensing element. The reversible pH sensor exhibited a visible transition from yellow to red as pH increased from acidic to near-neutral values, reflected by an increased B/G ratio. The irreversible pH sensor showed no visible change under these conditions, consistent with the pH range remaining below its transition threshold (~7.5–8.0). The uric acid sensor transitioned from colorless to pink with increasing uric acid concentration, as captured by rising ΔSaturation values. The glucose sensor displayed a progressive greenish shift correlated with higher glucose levels and increased |ΔGray| values. The moisture sensor exhibited a higher R/B ratio under AVF-P, corresponding to elevated humidity.

Finally, the robustness of the color-correction framework was validated using CIE XYZ values extracted under two illumination conditions (LED 3000 K and 5800 K). Six independent samples from each AVF group exhibited consistent color quantification across lighting environments (Fig. S12A–B). The corrected chromatic data correlated strongly with biomarker concentrations (Fig. S12C), confirming stable and reproducible smartphone-based color readouts. Collectively, these results demonstrate that the integrated color-correction framework enables accurate, user-friendly, and multiplexed quantification of vaginal health biomarkers under realistic use conditions.

4. Conclusion

We developed a R2R fabricated, fabric-based fluidic colorimetric sensor patch designed for seamless integration into commercial sanitary pads, enabling multiplexed detection of biomarkers associated with vaginal health. Utilizing wax-based microfluidic patterning on

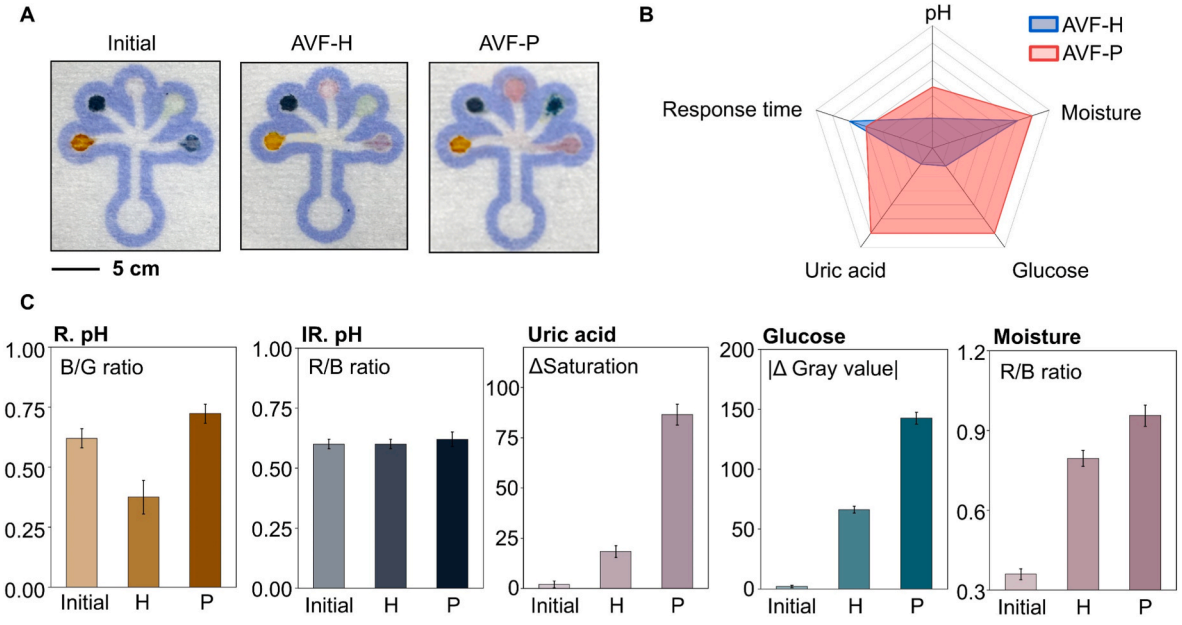

Fig. 5. Colorimetric sensing performance for artificial vaginal fluid (AVF) analysis. (A) Images of the sensor patch before fluid addition (initial) and after exposure to healthy (AVF-H) and pathological (AVF-P) formulations. (B) Radar plot summarizing the normalized responses of the five sensors under AVF-H and AVF-P conditions. (C) Quantitative analysis of colorimetric changes for each biomarker: reversible pH sensor, irreversible pH sensor, uric acid sensor, glucose sensor, and moisture sensor. All error bars represent the SD from three replicates.

nonwoven fabrics, the platform achieves scalable and low-cost fabrication of robust fluidic structures. Ink optimization with a mixed-solvent system (TEX/BEA) improved working time, eliminated the need for post-curing, and enhanced printing fidelity and barrier performance under continuous R2R conditions. The printed structures demonstrated reliable fluid confinement, consistent wicking behavior, and mechanical resilience suitable for wearable applications.

Unlike previous approaches that required customized substrates, our strategy allows direct integration onto widely used sanitary pads without altering their original form, offering a major advantage for user adoption and clinical translation. Colorimetric sensing performance was further enhanced through a regression-based model, enabling reliable signal quantification under variable imaging conditions. The sensor patch successfully distinguished between healthy and pathological artificial vaginal fluids (AVFs) within 10 min, with clear multiplexed color changes observable by both visual inspection and smartphone-based digital analysis.

This study presents a scalable, reproducible, and clinically relevant sensing platform with strong potential for low-cost, noninvasive monitoring of women's health. Nevertheless, several limitations should be acknowledged. The current evaluation was conducted using artificial vaginal fluids rather than clinical samples, which may not fully replicate the biochemical and rheological complexity of real secretions. Additionally, the present biomarker panel remains limited to pH, glucose, uric acid, and moisture, while other clinically relevant targets such as inflammatory cytokines, proteins, and microbial metabolites were not yet explored. Although material selection and encapsulation strategies were designed to minimize direct skin exposure, comprehensive safety assessments including skin irritation and sensitization testing will be important for clinical translation. Future work will therefore focus on expanding the biomarker panel, improving on-device stability for extended shelf life, conducting standardized safety evaluations, and validating diagnostic performance through clinical trials to accelerate translation toward practical applications in women's health monitoring.

CRediT authorship contribution statement

Ziheng Wang: Conceptualization, Data curation, Formal analysis, Investigation, Methodology, Validation, Visualization, Writing – original draft, Writing – review & editing. **Semin Kwon:** Formal analysis, Visualization. **Tianhao Yu:** Data curation. **Yumin Dai:** Visualization. **Young L. Kim:** Methodology. **Chi Hwan Lee:** Conceptualization, Formal analysis, Methodology, Project administration, Resources, Supervision, Writing – original draft, Writing – review & editing.

Declaration of competing interest

The authors declare that they have no known competing financial interests or personal relationships that could have appeared to influence the work reported in this paper.

Acknowledgement

This work was partially supported by the National Institutes of Health, National Eye Institute (NIH NEI) under grant R01EY034901 for the development of the colorimetric sensors, which is also utilized for fabricating the proposed devices. Additional support was provided by the Korea Institute for Advancement of Technology (KIAT) through funding from the Korea Government (Ministry of Trade, Industry and Energy, MOTIE) under the Global Industrial Technology Cooperation Center Support Program and the International Cooperative R&D Program (P0028319) for manufacturing process development. C.H.L. acknowledges support from the Leslie A. Geddes Endowment.

Appendix A. Supplementary data

Supplementary data to this article can be found online at https://doi.org/10.1016/j.bios.2026.118433.

Data availability

Data will be made available on request.

References

Ahmed, M.R., et al., 2023. Part. Part. Syst. Char. 40 (2), 2200153. https://doi.org/10.1002/ppsc.202200153.
Akkaynak, D., et al., 2014. J. Opt. Soc. Am. Opt Image Sci. Vis. 31 (2), 312–321. https://doi.org/10.1364/JOSAA.31.000312.
Baker-Rand, H., Kitson, S.J., 2024. Cancers 16 (5), 1028. https://doi.org/10.3390/cancers16051028.
Bianco, S., et al., 2013. J. Electron. Imag. 22 (2). https://doi.org/10.1117/1.JEI.22.2.023014, 023014-023014.
Black, K.I., Fraser, I.S., 2012. Int. J. Gynecol. Obstet. 119, S72–S75. https://doi.org/10.1016/j.ijgo.2012.05.002.
Cao, Y., et al., 2024. Am. J. Prev. Med. 67 (5), 698–704. https://doi.org/10.1016/j.amepre.2024.06.022.
Di Fiore, R., et al., 2021. Cancers 13 (3), 493. https://www.mdpi.com/2072-6694/13/3/493.
Dosnon, L., et al., 2025. Adv. Sci. 12 (32), e05170. https://doi.org/10.1002/advs.202505170.
Eskandar, K., 2024. J. Med. Clin. Nurs. Stud. 2 (1), 1–12. https://doi.org/10.61440/JMCNS.2024.v2.35.
Finlayson, G.D., et al., 2015. IEEE Trans. Image Process. 24 (5), 1460–1470. https://doi.org/10.1109/TIP.2015.2405336.
Gabrieli, D., et al., 2022. Diagnostics 12 (3), 574. https://doi.org/10.3390/diagnostics12030574.
Gil-Ibanez, B., et al., 2023. Int. J. Gynecol. Obstet. 33 (11), 1800–1806. https://doi.org/10.1136/ijgc-2023-004804.
He, R., et al., 2021. Adv. Sci. 8 (24), 2103030. https://doi.org/10.1002/advs.202103030.
Hung, P.-C., 1993. J. Electron. Imag. 2 (1). https://doi.org/10.1117/12.132391.
Kairys, N., et al., 2024. Bacterial vaginosis. StatPearls publishing, treasure Island, FL. https://www.ncbi.nlm.nih.gov/books/NBK459216/.
Kalantar-Zadeh, K., et al., 2024. ACS Sens. 9 (8), 3810–3827. https://doi.org/10.1021/acssensors.4c00567.
Kim, S.H., et al., 2021. Adv. Mater. 33 (44), 2104690. https://doi.org/10.1002/adma.202104690.
Li, Y., et al., 2024. Chin. Chem. Lett. 35 (7), 109220. https://doi.org/10.1016/j.cclet.2023.109220.
Liang, Y., et al., 2025. Int. J. Surg. 111 (1), 891–903. https://doi.org/10.1097/js9.0000000000001956.
Lin, H.-Y., et al., 2021a. Diagnostics 12 (1), 75. https://doi.org/10.3390/diagnostics12010075.
Lin, Y.-P., et al., 2021b. Diagnostics 11 (11), 1996. https://doi.org/10.3390/diagnostics11111996.
Luo, J., et al., 2025. Reprod. Biomed. Online, 104826. https://doi.org/10.1016/j.rbmo.2025.104826.
Maduta, C.S., et al., 2024. Trends Microbiol. 32 (3), 228–230. https://doi.org/10.1016/j.tim.2023.12.005.
Navarro, S., et al., 2023. BMC Microbiol. 23 (1), 186. https://doi.org/10.1186/s12866-023-02916-8.
Nguyen, H.H., et al., 2019. Materials 12 (1), 121. https://doi.org/10.3390/ma12010121.
Owen, D.H., Katz, D.F., 1999. Contraception 59 (2), 91–95. https://doi.org/10.1016/S0010-7824(99)00010-4.
Paghi, A., et al., 2023. Adv. Mater. Technol. 8 (8), 2201600. https://doi.org/10.1002/admt.202201600.
Pal, A., et al., 2020. Biosens. Bioelectron. 160, 112206. https://doi.org/10.1016/j.bios.2020.112206.
Park, S.M., et al., 2025. Sci. Adv. 11 (23). https://doi.org/10.1126/sciadv.adt4831 eadt4831.
Pascale, D., 2006. https://api.semanticscholar.org/CorpusID:36941390.
Prabhu, A., et al., 2021. ACS Omega 6 (19), 12667–12675. https://doi.org/10.1021/acsomega.1c00806.
Puggioni, G., et al., 2019. Sensors 19 (2), 422. https://doi.org/10.3390/s19020422.
Saraf, V.S., et al., 2021. Arch. Microbiol. 203 (7), 3793–3802. https://doi.org/10.1007/s00203-021-02414-3.
Shen, C.-J., et al., 2021. J. Healthc. Eng. 2021 (1), 4948954. https://doi.org/10.1155/2021/4948954.
Stabile, G., et al., 2021. Gels 7 (4), 157. https://doi.org/10.3390/gels7040157.
Stojanović, G.M., et al., 2025. IEEE Sens. Lett. 9 (4), 1–4. https://doi.org/10.1109/LSENS.2025.3549185.
Tzianni, E.I., et al., 2024. Talanta 269, 125475. https://doi.org/10.1016/j.talanta.2023.125475.
Wang, Z., et al., 2025. Adv. Healthcare Mater., e01998 https://doi.org/10.1002/adhm.202501998.

Whitbread, A.L., et al., 2024. J. Clin. Med. 13 (23), 7212. https://doi.org/10.3390/jcm13237212.
Wijeratne, D., et al., 2024. Int. J. Gynecol. Obstet. 164 (3), 1151–1159. https://doi.org/10.1002/ijgo.15211.
Zaheer, A., et al., 2024. Ann. Med. Surg. 86 (8), 4591–4600. https://doi.org/10.1097/ms9.0000000000002261.
Zhang, X., et al., 2020. Process Biochem. 99, 21–26. https://doi.org/10.1016/j.procbio.2020.08.012.
Zheng, X.T., et al., 2023. Sci. Adv. 9 (24). https://doi.org/10.1126/sciadv.adg6670 eadg6670.
Zheng, X.T., et al., 2024. Adv. Healthcare Mater. 13 (3), 2302173. https://doi.org/10.1002/adhm.202302173.
Zhu, B., et al., 2024. J. Glob. Health 14, 04155. https://doi.org/10.7189/jogh.14.04155.